Article

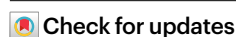# Selective formaldehyde condensation on phosphorus-rich copper catalyst to produce liquid C_{3+} chemicals in electrocatalytic CO_2 reduction

Check for updates

Minjun Choi [1,2,3], **Sooan Bae**[1,2,3], **Yeongin Kim**[1,2], **Youjin Lee**[1,2,3], **Mokyeon Cho** [1,2], **Sinwoo Kang** [1,2,3] & **Jaeyoung Lee** [1,2,3]

Recent advancements in the CO_2 reduction reaction (CO_2RR) target multicarbon chemical production and scalable electrode designs for industrial applications. Here we introduce a zero-gap cell utilizing humidified gas-phase CO_2 and circulated alkaline media, achieving a Faradaic efficiency of 66.9% for C_{3+} products and a current density of −1,100 mA cm^{-2}. In situ spectroscopic analyses revealed formaldehyde as a key intermediate formed on copper oxide/hydroxide interfaces derived from a phosphorus-rich copper catalyst. Unlike conventional pathways based on dimerization of CO intermediates, our study selectively produces liquid-phase multicarbon products because of autonomous local pH variations under a weak alkaline microenvironment, with allyl alcohol as the dominant C_{3+} product. The high selectivity and efficiency for liquid products provide a substantial advantage for storage and transport, highlighting the scalability and practical feasibility of our approach, which offers a potential economically viable solution for CO_2 utilization. This development encourages the adoption of CO_2RR technologies in iron−steel and petrochemical industries to mitigate greenhouse gas emissions.

The urgent need to mitigate greenhouse gas emissions coupled with industrial demand for a broad range of chemicals necessitates innovative production methods[1]. This is particularly true for C_{3+} multicarbon products, defined as compounds with three or more carbon atoms, which are essential for various industrial applications. C_{3+} multicarbon products are traditionally produced through methods such as catalytic cracking, crude oil distillation and oligomerization[2,3]. However, these traditional methods rely heavily on fossil fuel feedstocks and require high pressures and temperatures, leading to substantial greenhouse gas emissions, environmental pollution and energy consumption[4].

In contrast, by utilizing CO_2, a notorious greenhouse gas, as the primary feedstock, electrochemical CO_2 reduction offers the prospect of a more sustainable alternative, especially when powered by renewable electricity sources such as wind or solar power[5–8]. This method operates under ambient or near-ambient conditions, reducing energy demands compared with traditional methods. Despite these important advantages, electrochemical methods face challenges such as low Faradaic efficiencies (FEs), slow reaction rates (low current densities) and catalyst stability issues. Moreover, the variety of products formed during electrochemical CO_2 reduction necessitates an energy-intensive

[1]Department of Environment and Energy Engineering, Gwangju Institute of Science and Technology, Gwangju, Republic of Korea. [2]International Future Research Center of Chemical Energy Storage and Conversion Processes (ifRC-CHESS), Gwangju Institute of Science and Technology, Gwangju, Republic of Korea. [3]Ertl Center for Electrochemistry and Catalysis, Gwangju Institute of Science and Technology, Gwangju, Republic of Korea. e-mail: jaeyoung@gist.ac.kr

separation process to achieve industrial purity standards for each hydrocarbon product.

Recent research has focused on addressing these challenges to enhance the industrial viability of the CO_2 reduction reaction (CO_2RR)[8,9]. For instance, the use of gas diffusion electrodes (GDEs) in electrolytic cells has been explored to establish triple-phase boundaries by incorporating gaseous CO_2 inlets and liquid-phase alkaline catholytes into membrane electrode assembly (MEA) cells[10–13]. Despite considerable progress—for example, MEA cells have attained a heightened maximum current density (J_{max}) of 1.4 A cm^{-2}—obstacles remain, due in particular to the conversion of input CO_2 reactant into bicarbonate, resulting in carbonate deposition within the GDEs[2,13,14]. Additionally, although some systems have demonstrated direct conversion of CO_2 into C_{3+} hydrocarbons, their FEs remain below 20%, with current densities also typically falling below the industrially necessary level of 1 A cm^{-2} (refs. 15–17).

To overcome these limitations, we developed an approach that utilizes copper phosphide (CuP_2) cathodes paired with non-precious-metal anode catalysts in a zero-gap MEA configuration for the CO_2RR. With humidified CO_2 as the source for CO_2 electrolysis, we achieved successful operation at high current densities of up to −1.1 A cm^{-2} and a high partial current density of 735.4 mA cm^{-2} with a FE of 66.9% for C_{3+} products on a 9-cm^2 electrode. Using a larger electrode, we obtained a 30-fold increase in yield rate (µmol cm^{-2} h^{-1}) compared with previous studies[2,10,11,15,16,18,19]. Analytical techniques, including time-of-flight secondary ion mass spectrometry (ToF-SIM) and in situ Raman spectroscopy, revealed catalyst reconstruction involving copper oxide/hydroxide formation, demonstrating the potential of this approach to advance CO_2 reduction technologies.

Results

CO_2 electroreduction in zero-gap MEA configuration

The CO_2 supply is a critical factor that markedly influences the electrochemical reduction of CO_2 (ref. 20). Supplying humidified CO_2 is more effective than using its dry gaseous form[21]. This is because water vapour in the humidified CO_2 facilitates the conversion of CO_2 into hydrocarbons by improving mass transport and ensuring an adequate supply of reactants at the electrode surface[22]. Additionally, humidification can enhance ion conductivity and proton availability within the cell, thereby promoting reaction kinetics[23,24]. This method reduces the thickness of the CO_2 diffusion layers, thereby enabling the application of higher current densities. Utilizing humidified CO_2 ensures a consistent and abundant supply, optimizes the conditions for efficient electrochemical reduction, and enhances the current density[2,20]. To minimize the CO_2 diffusion layer on the surface of the electrode for high-current operation, humidified CO_2 was supplied to the cathode, as depicted in Fig. 1a. This technique enhances CO_2 transfer, leading to increased partial current density and FE even at low cell voltages. Moreover, this method makes it possible to achieve a considerably higher concentration of liquid multicarbon products by providing dissolved CO_2 with minimal water content[25].

Initially, a CuP_2 catalyst airbrushed onto a gas diffusion layer was used, and various anode catalysts were compared (see Methods for detailed procedures)[26]. In this study, CO_2 reduction experiments were conducted using a zero-gap MEA-type cell (Fig. 1a) with an electrode area of 9 cm^2. We used chronopotentiometry with a humidified CO_2 supply for CO_2 reduction. CO_2 electrolysis performance was evaluated by analysing the effluent gases and liquid products at room temperature and atmospheric pressure, specifically by calculating the FE values of the C_{3+} liquid products at various applied currents.

We first assessed the performance of CO_2 reduction using the widely recognized Pt/C catalyst and evaluated the performance of the zero-gap MEA-type cell. An experiment was conducted to determine the extent of cell voltage reduction with the inclusion of Pt/C on the anode side (Fig. 1b). We applied current densities (J) of −20 mA cm^{-2} to −200 mA cm^{-2} at −20 mA cm^{-2} intervals, with each stage conducted

for over 10 min. The cell voltage remained stable up to −140 mA cm^{-2}; beyond this range, it showed considerable instability with pronounced fluctuations.

Given the low stability, high cell potential and the use of precious-metal Pt/C, numerous researchers are actively working on replacing oxygen evolution reaction (OER) catalysts with non-precious-metal alternatives[27,28]. Hence, we experimented with non-precious-metal NiFe catalysts, which demonstrated competitive performance compared with Pt/C. The cell voltage when using NiFe was substantially lower than that of Pt/C and remained stable even at −200 mA cm^{-2} (Fig. 1c). When the type of anode was varied, the cell potential was the highest for Pt/C, followed by NiFe and iridium black (11). Nevertheless, NiFe proved to be the most stable anode, maintaining a constant voltage for 2 h even at an increased current density of −200 mA cm^{-2}.

During our investigation of the CO_2RR, most of the products on our catalysts were liquid phase. Consequently, our analysis and subsequent discussions primarily concentrate on the performance of the CO_2RR with respect to these liquid-phase products. Pt/C was used as the anode, and a current density of −100 mA cm^{-2} was applied for a duration of 2 h. Under these conditions, the FEs for the C_{2+} product spectrum revealed pronounced selectivity towards allyl alcohol, which comprised 48.7% of the total products (Supplementary Table 1). Within the array of C_{2+} products, the FEs for C_{3+} products were even more remarkable, exceeding 50% and reaching 56.0%.

When NiFe was used as the anode, the selectivity shifted towards C_2 products such as acetaldehyde and ethanol, rather than C_{3+} products, such as propionaldehyde, propanol, allyl alcohol and butyraldehyde, as shown in Supplementary Table 1. This shift occurred even though the same current density was applied as used with the Pt/C anode. The cell voltage provided by NiFe was insufficient to achieve high selectivity for C_{3+} products, suggesting that the anode material substantially influences product distribution.

To further investigate this phenomenon, additional experiments using a three-electrode system were conducted to discern the effect of anode potential variations on the working electrode (Supplementary Fig. 2a,b). CuP_2 was used as the working electrode, with Pt/C and NiFe as counter-electrodes. The results indicated that the choice of counter-electrode material influenced the reduction current at the working electrode. Specifically, when NiFe was used, the system exhibited a lower overpotential for the OER, leading to a lower cell voltage. This change in cell voltage affected the reduction potential at the cathode, thus altering the CO_2RR selectivity. These findings underscore that the nature of the anode catalyst could impact the electrochemical environment at the cathode, subsequently affecting the product distribution.

All performance evaluations were conducted using a two-electrode system with chronopotentiometry, applying a constant current density and measuring the resulting cell voltage. The cell voltage reflects contributions from both the anode and cathode. The difference in OER potentials between Pt/C and NiFe alters the reduction potential at the cathode. NiFe exhibits a lower overpotential than Pt/C in alkaline media (Supplementary Fig. 2c), meaning the cell voltage required for the OER with Pt/C would be higher. This increased anode potential affects the reduction environment at the cathode, influencing the selectivity of the CO_2 reduction products. Thus, the observed variation in product selectivity could be attributed to the different OER potentials of the anode catalysts, altering the electrochemical environment.

We also conducted linear sweep voltammetry (LSV) measurements in 0.5-M $KHCO_3$ electrolyte under both argon and CO_2 purging conditions, observing lower current densities under CO_2 purging (Supplementary Fig. 2d). This suggests that the CO_2RR dominate over the HER due to the formation of surface intermediates that inhibit the HER. Despite CuP_2's inherent activity for the HER, as evidenced by the free energy of hydrogen adsorption, the catalyst favours CO_2RR in the
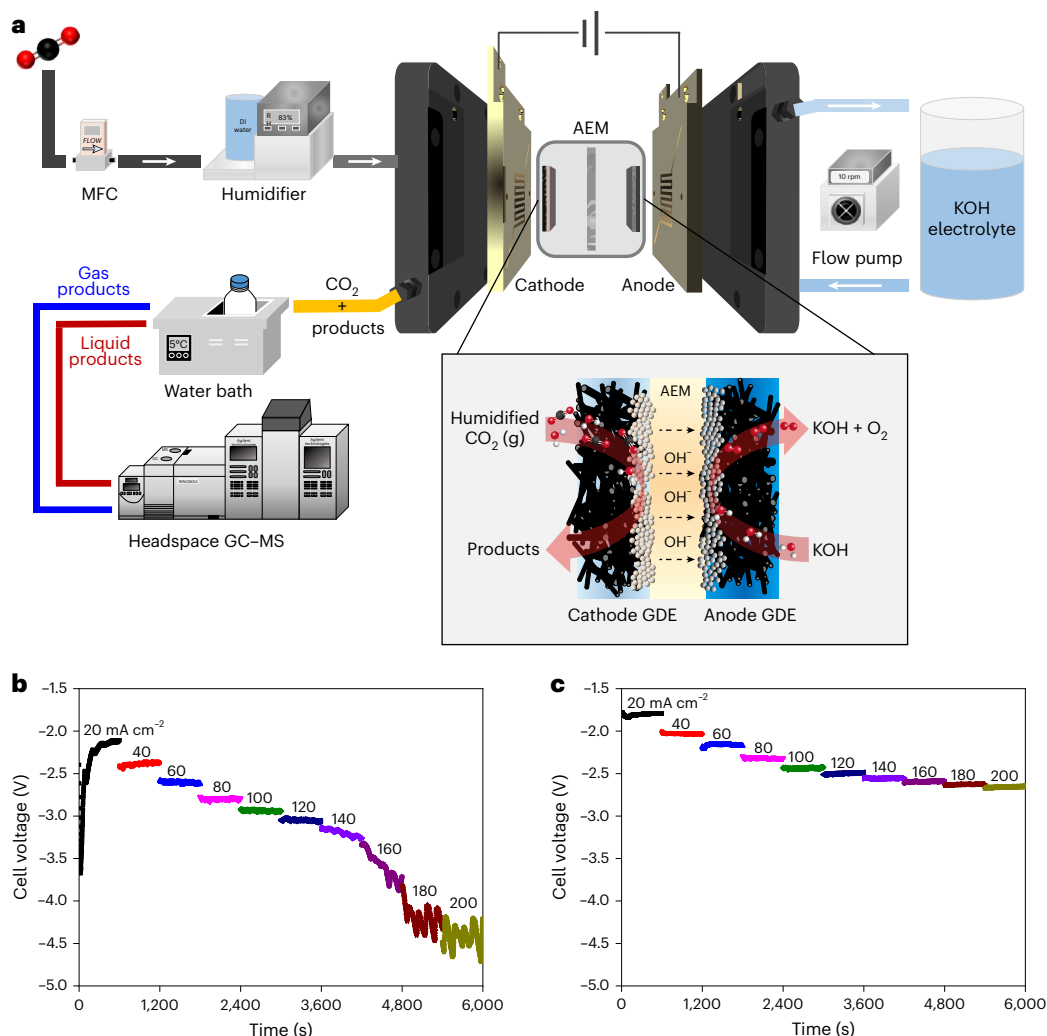
Fig. 1 | CO_2 electrolysis system for multicarbon production. a, Schematic illustration of humidified CO_2 supply to CO_2-to-C_{3+} systems, including the MEA with an anion-exchange membrane (AEM) and GDEs. The system uses a mass flow controller (MFC) to regulate the CO_2 flow at 500 sccm, maintained at 5 °C in a water bath, with product analysis conducted via headspace GC–MS. The anolyte, 1-M KOH, is circulated using a glow pump. **b**, Chronopotentiometric cell voltage profile using platinum on carbon (Pt/C) as an anode on a 9-cm² electrode, showing the voltage response to step changes in applied current density at 20, 40, 60, 80, 100, 120, 140, 180 and 200 mA cm⁻², measured at room temperature every 10 min. **c**, Chronopotentiometric cell voltage profile using nickel–iron (NiFe) as an anode on a 9-cm² electrode, showing the voltage response to step changes in applied current density at 20, 40, 60, 80, 100, 120, 140, 180 and 200 mA cm⁻², measured at room temperature every 10 min.

presence of CO_2, with intermediates blocking active sites for the HER and promoting C–C coupling reactions. These results underscore the catalyst's selectivity towards multicarbon product formation under CO_2RR conditions.

Reconstruction of CuP_2 catalyst under CO_2RR conditions

To delineate the alterations in the cathode catalyst due to CO_2 electrolysis, we used various analytical techniques. A ToF-SIMS analysis of the as-prepared CuP_2 catalyst (Fig. 2a,b) revealed that the CuP_2 surface was predominantly coated with phosphate species[26,29]. Even in the unreacted catalyst, the high oxygen affinity of phosphorus allows oxygen to permeate, resulting in a superficial phosphate layer.

A complementary line-profiled scanning electron microscopy with energy-dispersive X-ray spectroscopy (SEM-EDS) analysis, shown in Supplementary Fig. 3a, corroborates the presence of a phosphate layer on the surface. After the CO_2RR experiments, a discernible reconstruction of the surface, manifesting as a compositional shift, was observed. The initially thin phosphate layer progressively diminished, and was supplanted by an emerging oxide layer, as shown in Fig. 2d,e by ToF-SIMS analysis. This transition was parallel to the line-profiled

SEM-EDS pattern (Supplementary Fig. 3), where oxides became predominant at sites formerly occupied by phosphates. This CO_2RR process suggests that the high oxygen affinity of phosphorus catalyses the surface reconstruction of the catalyst.

For a more detailed analysis, we used identical-location scanning electron microscopy (IL-SEM) (Fig. 2c,f). This technique makes it possible to observe the same particles before and after the reactions. A marked increase in the oxygen wt% and a corresponding decrease in the phosphorus wt% postreaction, aligning with earlier findings, substantiated the inferred catalyst modifications and confirmed the occurrence of prominent catalytic changes (Supplementary Table 2).

X-ray photoelectron spectroscopy (XPS) was performed to investigate the chemical bonding on the catalyst surface (Supplementary Fig. 4). The phosphorus 2p spectrum of the as-prepared CuP_2 electrode revealed two distinct doublets. The peak at 134.3 eV corresponds to oxidized phosphorus (phosphate), indicating a hydrated phosphate layer on the surface, consistent with previous findings. After the CO_2RR, a hydroxylated phosphate layer formed. The peak at 129.7 eV, lower than red phosphorus at 130.2 eV, suggests charge transfer between copper and phosphorus, with phosphorus being
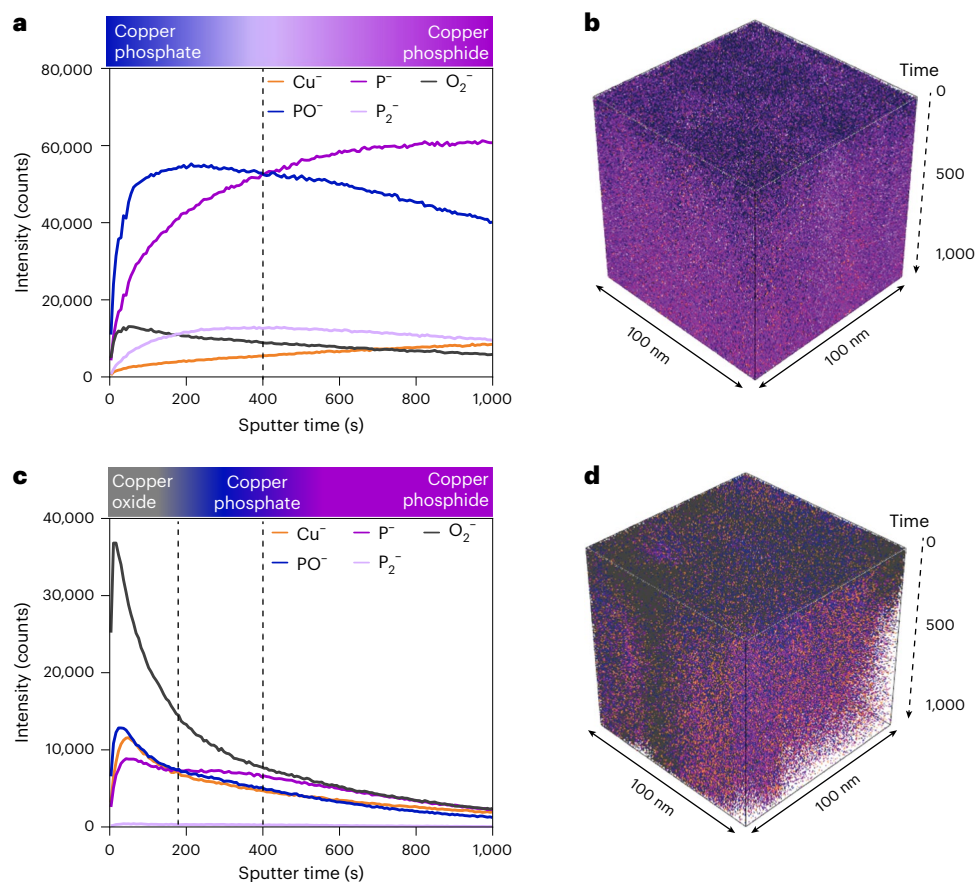
Fig. 2 | Surface states of the CuP$_2$ catalyst before and after the CO$_2$RR. a,c, ToF-SIMS negative-ion depth profile and IL-SEM of a CuP$_2$ cathode sample before the CO$_2$RR (**a**) and after the CO$_2$RR (**c**). All ions (Cu$^-$, P$^-$, O^{2-}, PO$^-$ and P^{2-}) are indicated on the profile. **b,d,** ToF-SIM 3D plots of each ion before the CO$_2$RR (**b**) and after the CO$_2$RR (**d**).

negatively charged. Comparing spectra before and after the CO$_2$RR, the intensity of the phosphorus $2p^{3/2}$ peak increased, indicating the persistence of phosphide postreaction. Additionally, the oxygen 1s spectra showed a decrease in the P–O interaction peak intensity and an increase in the Cu–O interaction peak intensity after the CO$_2$RR. These changes highlight notable surface chemistry modifications due to the reaction.

Although previous analyses were performed ex situ, leading to concerns about potential surface oxidation postreaction due to air exposure, we investigated surface changes during the CO$_2$RR using in situ Raman spectroscopy. A custom-built cell designed for a three-electrode H-cell configuration (Supplementary Fig. 5) was used for these experiments[30]. A constant potential of −0.6 V$_{RHE}$ (RHE, reversible hydrogen electrode) was applied for 2 h, and the spectra were sequentially acquired to monitor temporal changes under a CO$_2$-saturated atmosphere.

The initial observations at an open-circuit potential indicated the presence of a phosphate layer on the electrode surface, as shown in Fig. 3. Upon application of the potential, we observed a gradual decrease in the intensity of the peaks associated with Cu$_3$(PO$_4$)$_2$ at specific wavenumbers (1,361, 1,595 cm^{-1}), suggesting the depletion of the phosphate species. Concurrently, peaks corresponding to CuO and CuO$_x$/(OH)$_y$ (389–394 cm^{-1}) emerged, indicating the formation of copper oxide and hydroxide species[31]. This transition in the Raman spectra signifies the ongoing reconstruction of the catalyst surface during the CO$_2$RR. To ensure the reliability of our findings and confirm the reproducibility of the observed surface transformations, Raman spectra were collected from multiple locations (≥3) across all samples and under each potential investigated in this study.

We investigated the electrochemical stability of CuP$_2$ across various pH levels and potential conditions, focusing on the relevant operational range for CO$_2$ reduction reactions—specifically, the stability region for CuP$_2$ within a pH range from neutral to slightly alkaline, which corresponds to the local conditions during the CO$_2$RR as OH$^-$ ions are generated, shifting the local pH towards more alkaline conditions. Within this defined stability region, CuP$_2$ remains robust, avoiding considerable degradation or dissolution[32]. This is corroborated by the formation of stable CuP$_2$ and other protective species, such as phosphate layers, which help mitigate corrosion and maintain the catalyst's integrity.

Based on our results, we observed that CuP$_2$ initially maintains a stable structure under CO$_2$RR conditions but undergoes surface reconstruction as the reaction progresses. It is important to distinguish between reconstruction and degradation. The high oxophilicity of CuP$_2$ leads to strong interactions with oxygen species, resulting in a gradual transformation of the surface to Cu$_x$P$_y$O$_z$ (copper phosphate) phases, eventually progressing to copper oxide and finally to metallic copper. Despite this reduction to copper, phosphate groups remain on the surface, actively contributing to the catalyst's performance and aiding in multicarbon product formation. This surface reconstruction aligns with the behaviour of Cu$_2$O-derived copper catalysts, where the formation of active copper metal sites is beneficial for C$_{2+}$ product selectivity.

Furthermore, the stability test conducted at a high current density of 500 mA cm^{-2} for 60 h demonstrated a consistent cell voltage with minimal fluctuations (Supplementary Fig. 6). This consistent voltage profile indicates that the postreconstruction catalyst maintains a robust structure without signs of marked degradation, as any degradation would have led to noticeable voltage instability. The reconstructed,
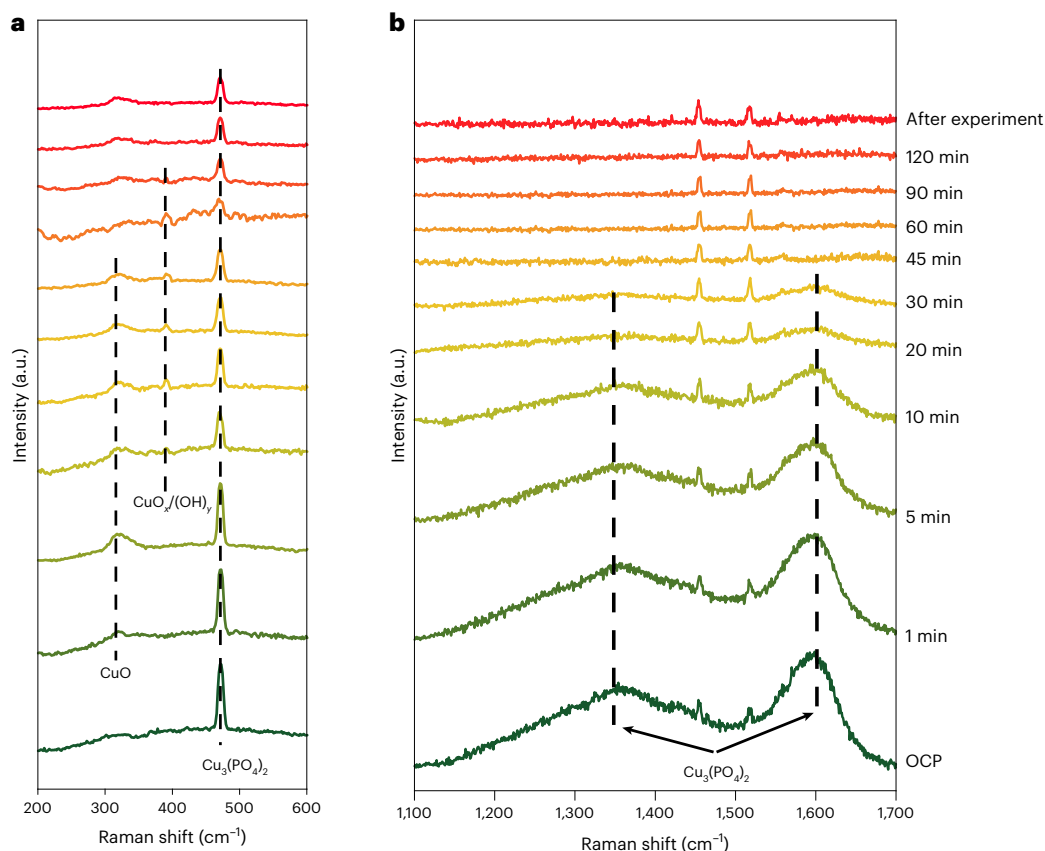
Fig. 3 | In situ Raman spectroscopy results over time. a, Copper oxide region of the reconstructed CuP_2 electrode. **b**, Copper phosphate/phosphide region of the reconstructed CuP_2 electrode. The measurements were conducted under a constant potential of $-0.6\ V_{RHE}$, with a total charge of -3.44 C applied for 45 min.

CuP_2-derived catalyst, featuring surface-bound phosphate groups, provides a stable and optimal environment for CO_2 reduction, differentiating it from conventional copper catalysts that start in their metallic state. This unique reconstruction pathway enhances the catalyst's ability to promote multicarbon coupling reactions, highlighting the critical role of phosphate groups in stabilizing the surface and maintaining catalytic activity.

Proposed CO_2RR pathway for multicarbon product generation
Drawing from the detailed analysis of the conversion ratios in Fig. 5e, and reinforcing the mechanisms discussed in our previous work, we highlight a distinct pathway in CO_2 electrolysis, leading to multicarbon products that do not primarily rely on CO intermediates and C–C dimerization. Diverging from the traditional focus on CO dimerization, our findings emphasize a formaldehyde-driven condensation mechanism as the initial step in C–C coupling[26,29,33].

To elucidate the role of formaldehyde in the CO_2RR, we carried out additional experiments comparing the reduction of CO, CO_2 and formaldehyde under similar conditions. These experiments were performed using a microfluidic GDE cell (Supplementary Fig. 7) at a potential of -0.6 V versus RHE. For the reduction of CO and formaldehyde, we used a phosphate buffer solution saturated with argon to exclude CO_2 participation. However, for CO_2 reduction, a 0.5-M $KHCO_3$ solution saturated with CO_2 was used.

As shown in Supplementary Fig. 8, CO reduction did not yield any carbon products, whereas CO_2 reduction produced formate, acetaldehyde and butanol, consistent with a previous report[26]. Formaldehyde reduction led to a slight increase in hydrogen production and a substantial increase in selectivity towards C_{2+} compounds, specifically acetaldehyde and butanol. Although the product distribution might differ from that in an MEA-type cell, the enhanced selectivity for multicarbon

compounds during formaldehyde reduction underscores its crucial role in the C–C coupling process during CO_2 reduction. These findings support the hypothesis that formaldehyde is a key intermediate in forming multicarbon products, highlighting its importance in the overall reaction mechanism.

To further explore our proposed mechanism, we outline several tentative steps, detailed in Supplementary Fig. 10: surface protonation, CO_2 adsorption, rearrangement of CO_2 and formation of formate, formate coverage at the CuP_2 surface, and formaldehyde formation and aldehyde formation. The literature suggests that the Gibbs free energy (ΔG) values for these steps may be negative, indicating potential thermodynamic favourability, although this is based on preliminary evidence from previous studies[29,34–36]. At this stage, our working hypothesis for the mechanism is tentatively supported by these observations, but this will require additional experimental and computational investigations to confirm its validity.

As proposed in Supplementary Fig. 11a, in the initial step for CO_2^- binding, carbon-binding leads to CO formation, which can further go through CO dimerization to produce multicarbon products such as ethylene, ethanol, 1-propanol, etc. Oxygen binding, however, leads to the formation of formate, which is widely accepted as an end product. In the presence of Lewis acid catalysts, formaldehyde self-condensation can be catalysed to form the C_2 compound known as glycolaldehyde. Some non-copper catalysts with Lewis acid sites have been proposed for the self-condensation of formaldehyde as a C_{2+} formation mechanism.

To further investigate the differences in C–C coupling mechanisms and validate the reaction pathways illustrated in Supplementary Fig. 11a, and to demonstrate the related intermediates of formaldehyde condensation shown in Supplementary Fig. 9, we conducted in situ surface-enhanced infrared absorption spectroscopy (SEIRAS) experiments. These experiments aimed to investigate the adsorption
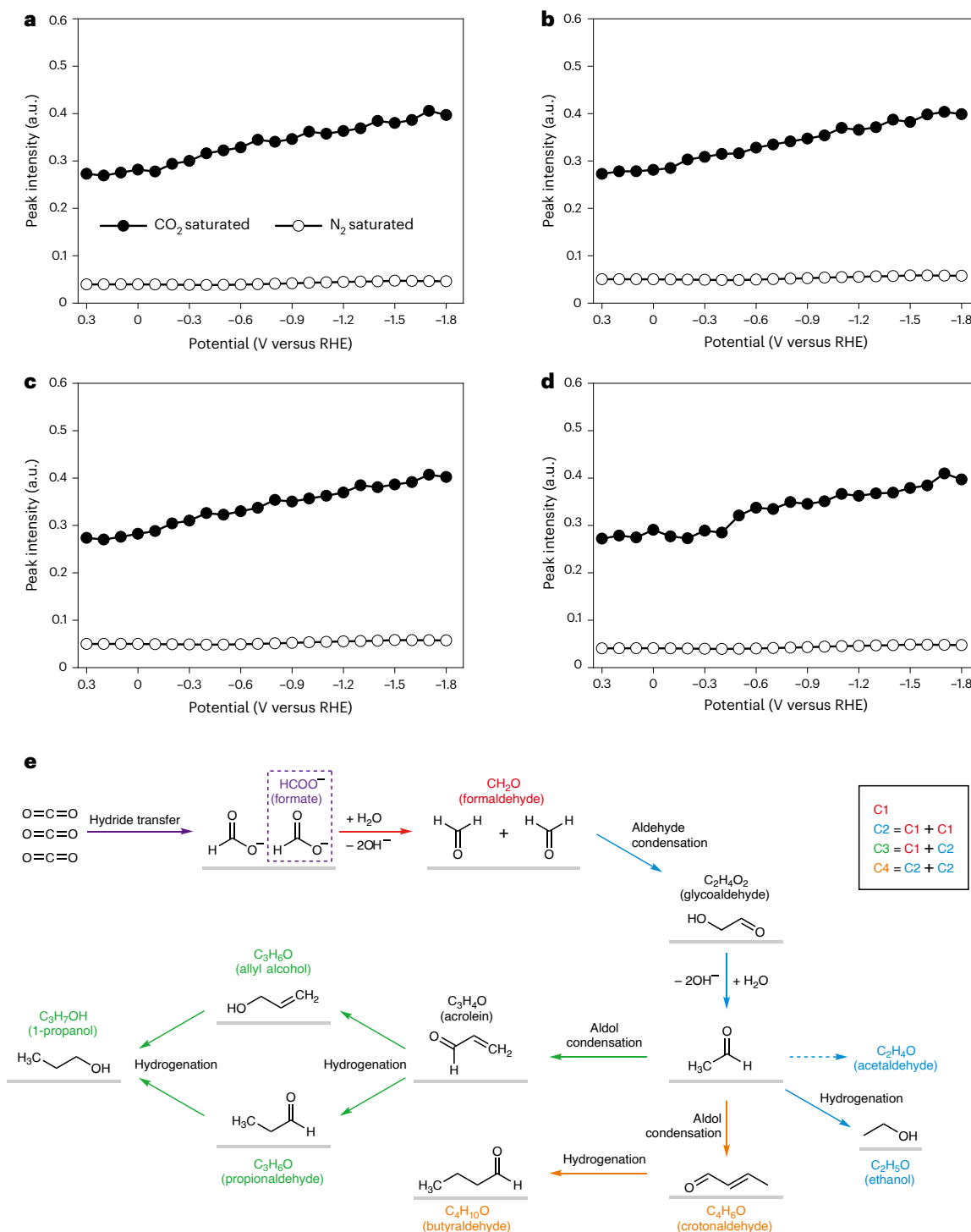
Fig. 4 | In situ SEIRAS spectrum and proposed reaction pathways of CO_2 to each product. a–d, $HCOO_{ad}$ (**a**), HCO_{ad} (**b**), OCH_{3ad} (**c**) and OC_2H_{5ad} (**d**) intermediates identified by in situ SEIRAS, related to the formaldehyde condensation reaction as a C–C coupling process. **e,** Proposed reaction pathways to various products, with colour coding for carbon chain length: C_1 (purple/red), C_2 (blue) C_3 (green), C_4 (orange).

behaviour of CO on metallic copper and CuP_2 surfaces under applied reduction potentials. As shown in Supplementary Fig. 11c,d, metallic copper exhibited a clear CO adsorption peak (*CO_{ad}) under reduction conditions, confirming its role in CO dimerization pathways that lead to multicarbon products. In contrast, CuP_2 showed no detectable CO adsorption peaks across the entire range of applied potentials ($0.3\,V_{RHE}$ to $-1.8\,V_{RHE}$), indicating a fundamentally different reaction mechanism. These results validate the proposed reaction pathways, where CuP_2 avoids the CO-mediated C–C coupling, and instead support

alternative routes, such as the formate pathway, for multicarbon product formation. The majority of formate-producing catalysts that require high overpotentials are known to form a curved structure of CO_2 during the reaction, which is bound to oxygen atoms on the surface of the catalyst through a proton-coupled electron transfer process. This mechanism is consistent with our previous XPS results, which demonstrate that charge transfer takes place between copper and phosphorus. This suggests that copper has a positive charge and could potentially act as a hydride acceptor in the hydride transfer
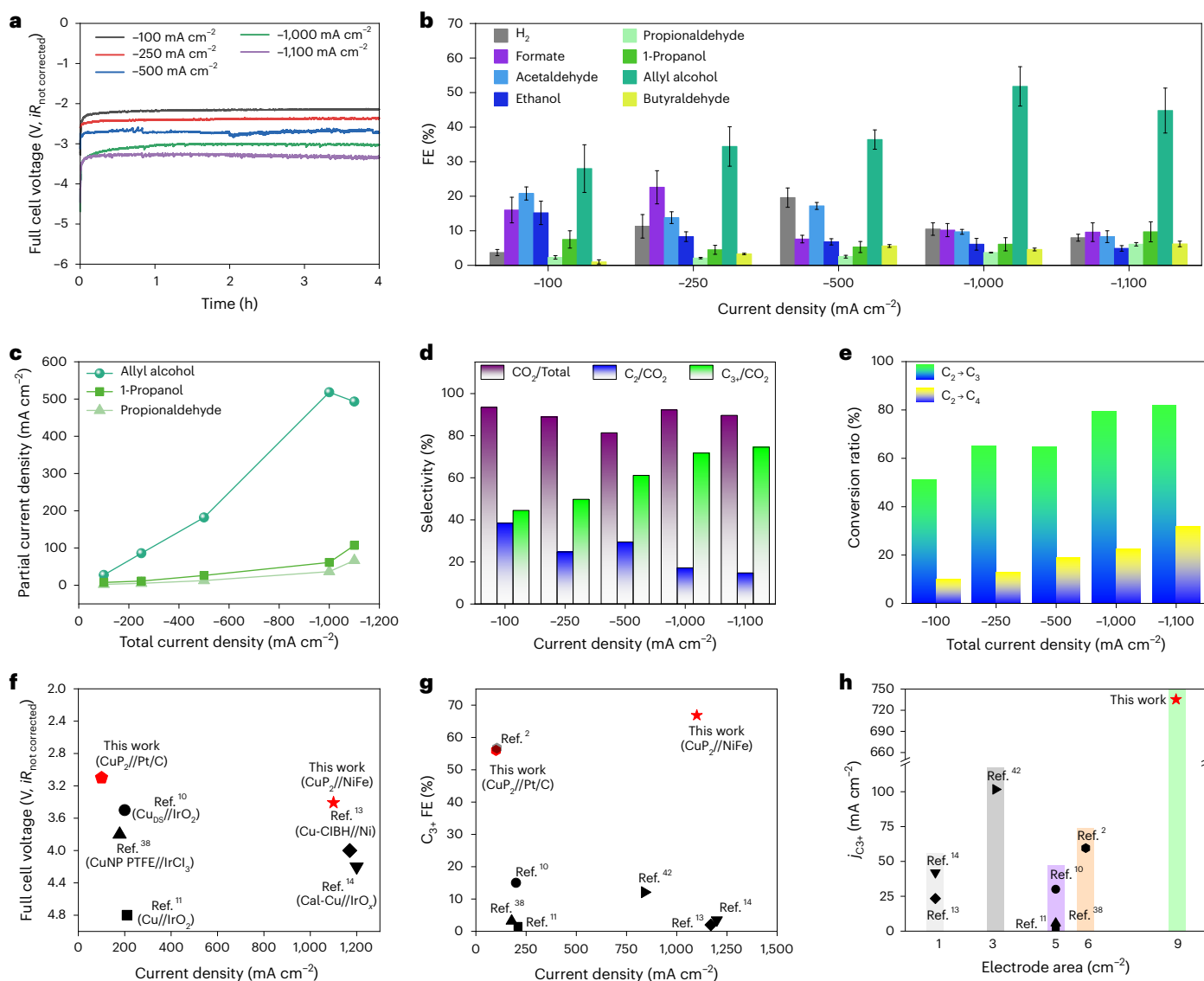
Fig. 5 | Electrochemical performance and product analysis of CO_2.
a, Stability of full-cell voltage over time across a range of current densities from -100 mA cm^{-2} to -1.1 A cm^{-2}. **b**, FEs for different products at specified current densities. **c**, Partial current densities for C_3 products (allyl alcohol, 1-propanol and propionaldehyde) plotted against total applied current density. **d**, Selectivity comparison for C_{1-4}, C_2 and C_{3+} products relative to CO_2 reduction at different current densities. **e**, Conversion rate of CO_2 into C_1–C_4 products at varying current densities. **f**, Comparison of full-cell voltage under no iR

correction conditions across different studies including this work, for various current densities. Cal-Cu, cation-augmenting layer modified copper. **g**, FE of C_{3+} products against total current density in comparison to other studies. **h**, Product yield function against electrode area, demonstrating the scalability of the methodology in this work and other studies (detailed in Supplementary Table 4). The FE values are means, and error bars represent the s.d. from three independent measurements ($n = 3$).

mechanism ($CO_2 + H^- \rightarrow HCOO^-$) producing formate, which is confirmed in Fig. 4a for HCOO$_{ad}$. After HCOO$_{ad}$ adsorption, the reaction can proceed through HCO$_{ad}$ to form formaldehyde (Fig. 4b). Under mild conditions, it is energetically favourable for two molecules of formaldehyde to undergo self-condensation and form a C–C bond. This reaction has a standard Gibbs free energy of -25 kJ mol^{-1}. During the formaldehyde condensation reaction, OCH$_{3ad}$ (Fig. 4c) appears after the carbon atoms are coupled, and eventually the OC$_2$H$_{5ad}$ (Fig. 4d) intermediate is formed, which is a primary intermediate for acetaldehyde. The onset of the OC$_2$H$_{5ad}$ intermediate starts slightly behind the other intermediates which means it appears after the C–C coupling reaction.

In this refined pathway (Fig. 4e), the decreased amount of C_2 intermediates steers the reaction towards formaldehyde condensation, yielding acetaldehyde[37–40]. This compound, together with formaldehyde, undergoes an aldol condensation reaction facilitated

by specialized catalysts to form acrolein, a key intermediate of C_3 products. This pathway bifurcates with the hydrogenation of acrolein, resulting in the formation of allyl alcohols and propionaldehydes. Subsequent hydrogenation leads to the synthesis of 1-propanol[41,42].

Moreover, in line with the reaction schemes outlined in our earlier studies, the aldol condensation of two acetaldehyde molecules led to the production of butyraldehyde, a C_4 compound. This clearly illustrates that the electrochemical conversion of CO_2 to multicarbon chemicals involves a complex interplay of reactions, highlighting formaldehyde condensation as a pivotal step in the formation of higher-order carbon products.

By emphasizing the role of formaldehyde in this study, we aimed to refine the understanding of multicarbon product synthesis from CO_2 and provide insights that can lead to the development of more efficient catalytic systems for CO_2 utilization.

High current density electrochemical CO_2 reduction performance

Following on from the electrolysis system described in Fig. 1a, we conducted a series of experiments under current densities of -100 mA cm^{-2} to -1.1 A cm^{-2}. We monitored the full-cell voltage under a constant current density for 4 h using non-precious-metal catalysts on both the cathode and anode, as illustrated in Fig. 5a. The cell potential remained stable across all current densities, maintaining -3.4 V at -1.1 A cm^{-2} without any *iR* correction, as further detailed in Supplementary Fig. 12. Hydrogen was the predominant gaseous product, accompanied by a spectrum of CO_2RR liquid products (Fig. 5b and Supplementary Table 3). Notably, allyl alcohol maintained the highest FE of 51.81% at a current density of -1 A cm^{-2}, underscoring its selectivity in our system. Concurrently, we detected the formation of C_1 compounds, such as formates, and C_2 compounds, such as acetaldehyde and ethanol. The trend for C_3 compound formation, specifically propionaldehyde and propanol, was equally promising, and butyraldehyde confirmed the presence of C_4 products.

To gain further insights into the cathodic environment and polarization potential at the CuP_2 working electrode under these operating conditions, we designed a modified zero-gap three-electrode cell. This set-up incorporated a reference electrode insertion point to directly measure the cathode polarization potential at various applied current densities. Chronopotentiometric experiments revealed a strong correlation between the cathode polarization potential and CO_2RR product selectivity. As shown in Supplementary Table 3 and Supplementary Fig. 13, the cathode polarization potential progressively shifted from -0.82 V versus RHE at -100 mA cm^{-2} to -1.12 V versus RHE at -1.1 A cm^{-2}. This shift in potential directly influenced product distributions, with lower potentials favouring C_1 and C_2 products and higher potentials promoting C_3 and C_4 product formation.

A closer analysis of the C_3 compounds revealed an escalating partial current density for allyl alcohol, 1-propanol and propionaldehyde, with the current density increasing up to -1.0 A cm^{-2}, as depicted in Fig. 5c. However, a subtle decrease in the quantity of allyl alcohol was observed upon increasing the current density to -1.1 A cm^{-2}. The selectivity trends for the C_2 and C_{3+} products relative to the total CO_2 reduction indicated a decline in C_2 and an enhancement in C_{3+} selectivity with increasing current density, as shown in Fig. 5d. This trend suggests a transitional pathway in which C_{3+} products are derived through a coupling reaction, such as aldol condensation, from C_2 intermediates.

Figure 5e shows the relationship between the C_2, C_3 and C_4 products, indicating that as the current density increases, discernible shifts occur from C_2 to C_3 and from C_2 to C_4. However, the transition from C_3 to C_4 (Supplementary Fig. 14) did not exhibit a consistent trend across varying current densities, indirectly substantiating that C_3 compounds originate from the coupling of C_2 and C_1, while C_4 compounds arise from C_2 coupling reactions rather than from C_3 and C_1. To further investigate the selectivity of CuP_2 in formaldehyde reduction and its role as an intermediate in C–C coupling, isotopic labelling experiments were performed using ^{13}C-labelled formaldehyde in an argon-saturated phosphate buffer solution (Supplementary Fig. 15). ^{13}C NMR analysis revealed distinct peaks corresponding to various C_1 and C_{2+} products, confirming the formation of methanol, acetaldehyde, propionaldehyde, ethanol, butyraldehyde and butanol. Notably, methanol was observed, which is attributed to the spontaneous conversion of formaldehyde under reaction conditions. This analysis provides direct evidence for the role of formaldehyde as a crucial intermediate in multicarbon product formation during the reduction process.

A comparative analysis of the product distributions obtained from formaldehyde reduction (Supplementary Fig. 16a) and the CO_2RR (Supplementary Fig. 16b) experiments highlights pronounced differences driven by the reaction microenvironment and variations in local pH influenced by the cell configuration. In the CO_2RR experiment using a MEA at high current density, products such as formate, acetaldehyde, ethanol, propionaldehyde, 1-propanol, allyl alcohol and butyraldehyde were detected. In contrast, the formaldehyde reduction experiment conducted at -0.9 V versus RHE in a flow cell predominantly yielded methanol, acetaldehyde, propionaldehyde, ethanol, butyraldehyde and butanol. The confined reaction zone in the MEA cell, with limited electrolyte presence, leads to rapid proton consumption and substantial changes in local pH near the catalyst surface. This environment favours C–C coupling reactions and facilitates the formation of multicarbon products. Conversely, the flow cell set-up, with a spacer creating a thicker electrolyte layer, results in a different local pH profile that stabilizes formaldehyde and promotes its reduction to methanol.

The combined use of headspace gas chromatography–mass spectrometry GC–MS and ^{13}C NMR analysis was crucial in identifying the complete product distribution. Headspace GC–MS (Supplementary Figs. 16a and 17), with its high sensitivity to volatile organic compounds, detected trace-level allyl alcohol, which was not observed in the ^{13}C NMR spectrum due to the latter's higher detection limit. This highlights the complementary nature of these analytical techniques and underscores the importance of using multiple methods to fully characterize the product profile, especially for trace-level products.

The observed differences in product selectivity emphasize the role of formaldehyde as an active intermediate in C–C coupling reactions. During the CO_2RR, formaldehyde is probably formed transiently on the catalyst surface but is rapidly consumed, facilitating the formation of higher-order products such as propionaldehyde and butyraldehyde. In the formaldehyde reduction experiment, however, the initial presence of labelled formaldehyde provided direct evidence of its nucleophilic activity, leading to methanol formation and enabling further C–C coupling to produce multicarbon alcohols. This demonstrates the high selectivity of CuP_2 for formaldehyde condensation, validating the proposed reaction mechanism and the catalyst's effectiveness in promoting C–C bond formation.

These findings illustrate the critical role of the reaction microenvironment and local pH variations influenced by cell configuration in determining product selectivity. The MEA cell configuration, with its confined reaction environment, promotes rapid C–C coupling and favours the formation of higher-order aldehydes and alcohols. In contrast, the flow cell set-up, with a different local pH profile, stabilizes formaldehyde as a key intermediate, promoting its direct reduction to methanol and subsequent multicarbon synthesis. This underscores the importance of formaldehyde in multicarbon product formation and highlights its pivotal role in C–C coupling pathways during CO_2RRs.

To address concerns about electro-osmosis at current densities exceeding -1.0 A cm^{-2}, we conducted additional experiments to analyse the anolyte for crossover products postelectrolysis. No products were detected in the anolyte, as detailed in Supplementary Fig. 18, indicating no notable electro-osmosis. Moreover, we monitored cell voltage over time while applying constant currents above -1.0 A cm^{-2}. Figure 5a shows no considerable voltage changes, confirming the absence of oxidation reactions due to crossover products. This stability confirms that our system effectively prevents product loss from electro-osmosis, ensuring reliable CO_2 reduction results.

To address concerns about potential anode material contamination affecting CO_2RR activity, we conducted several analyses and additional experiments. SEM energy-dispersive X-ray analysis on the cathode postreaction showed no deposition of nickel or iron (Supplementary Fig. 19). Additionally, inductively coupled plasma optical emission spectrometry (ICP-OES) analysis of the catholyte in CO_2RR experiments detected no nickel or iron ions (Supplementary Table 5).

To further validate our findings, we performed a model electrolysis experiment using the same NiFe anode and the same anion-exchange membrane, paired with a Pt/C cathode. We applied constant current densities of 1.1 A cm^{-2} and 3.0 A cm^{-2} for 4 h, periodically sampling the catholyte for any potential nickel or iron contamination (Supplementary Table 6).

The results of SEM energy-dispersive X-ray and ICP-OES analyses consistently showed no evidence of nickel or iron contamination on the cathode or in the catholyte. These findings confirm that the observed differences in CO_2RR activity are attributed to intrinsic catalytic properties and reaction conditions, rather than anode material contamination. This supports our claim that different anode materials result in different cell voltages, influencing the overall CO_2RR activity without cross-contamination effects.

As delineated in Fig. 5f, our findings, particularly at a high current density of -1.1 A cm^{-2}, showcased the lowest observed cell potential, outperforming even the Pt/C catalysts at equivalent current densities. Furthermore, when juxtaposed with other studies focusing on C_{3+} product yields[10,11,15,16,18] (Fig. 5g), our system exhibited remarkable selectivity for C_{3+} products, showing an impressive FE of 66.9%.

Theoretically, an increased electrode area should proportionally increase the yield of conversion products. However, in practice, upscaling the electrode area can introduce challenges such as increased surface resistance. Nonetheless, our research demonstrates that the strategic enlargement of the electrode area can substantially enhance the yield rate, as evidenced by the production volume exceeding that of other studies by more than 30 times (Fig. 5h). This reinforces the notion that optimizing the electrode microenvironment for CO_2 participation can markedly improve the efficiency of CO_2RRs.

Conclusions

Our comprehensive study illuminates a series of pathways for the electrochemical reduction of CO_2 to multicarbon compounds, leveraging non-precious-metal catalysts to optimize efficiency and selectivity. The experiments conducted not only demonstrated a stable cell potential across a wide range of current densities but also highlighted the robust selectivity for valuable C_{3+} compounds, particularly allyl alcohol, which achieved a FE exceeding 50%. These results, situated at the forefront of CO_2RR research, mark a step towards the sustainable production of chemicals.

In situ Raman spectroscopy revealed the dynamic surface transformations of the catalyst during the CO_2RR, offering a deeper understanding of the mechanisms at play. The emergence of copper oxides and hydroxides during the reaction provided clear evidence of the structural evolution of the catalyst, essential for guiding future catalyst designs. Our findings also shed light on the crucial intermediate role of C_2 compounds and the importance of aldol condensation reactions in the formation of higher-order alcohols and aldehydes. This insight underlines the complexity of the CO_2RR process and its potential to be harnessed for the targeted synthesis of specific products.

Additionally, in situ SEIRAS experiments were conducted to observe the intermediate species and support the reaction pathway. The SEIRAS results showed the formation of formate and subsequent formaldehyde on the catalyst surface, consistent with our proposed mechanism and highlighting the importance of these intermediates in the C–C coupling process.

Furthermore, our study challenges the traditional constraints associated with electrode area scaling. By strategically enhancing the electrode area, we achieved a remarkable increase in the product yield rate, outperforming existing benchmarks by approximately 30-fold in terms of yield rate (μmol cm^{-2} h^{-1}), as detailed in Supplementary Table 4, which compares our results with previous studies[2,10,11,15,16,18,19]. This not only confirms the viability of scaling up the CO_2RR but also emphasizes the importance of optimizing the electrode design to maximize reactant participation. This study marks an advancement in the electrochemical conversion of CO_2, providing a viable route to high-value multicarbon compounds with high selectivity and efficiency. Our methodology provides guidance for the development of scalable, sustainable and economically feasible CO_2RR technologies. The approach achieved a partial current density of 735.4 mA cm^{-2} and a FE of 66.9% for C_{3+} products, notably improving yield rates by approximately 30-fold compared with existing benchmarks (Supplementary Table 4), demonstrating a robust step forward in CO_2 reduction technologies.

Methods

Electrode preparation

The cathode catalysts were synthesized according to the method described in our previous study[26]. The catalyst ink was composed of 27 mg of the synthesized catalyst, 27 μl of an ionomer solution (PiperION Dispersion; 5 wt%) and 7,860 mg of isopropyl alcohol. The ink was thoroughly dispersed, and then, using N_2 as the carrier gas, was airbrushed onto a 3 cm × 3 cm gas diffusion layer (22BB, Sigracet). For the anode catalyst, nickel nitrate (Ni(NO$_3$)$_2$·6H$_2$O; 99.999%; Sigma-Aldrich) and iron chloride (FeCl$_2$·4H$_2$O; 99.99%; Sigma-Aldrich) were utilized in their as-received forms for the electrodeposition process. A 0.1-M solution of metal precursors was prepared by dissolving these salts in distilled water. The Ni^{2+} and Fe^{2+} compositions of the electrolytes were maintained at an optimized ratio of 9:1. The working electrode, consisting of stainless steel fibre paper (Bekipor ST 40BL3, Bekaert), was subjected to a constant current of -2.5 mA cm^{-2}. A carbon cloth was used as the counter-electrode. The deposition time was set to 7,200 s to achieve optimal performance.

Surface analysis methods

We analysed the catalyst surface by field emission SEM (Verios 5 UC, Thermo Fisher) to observe the morphological characteristics. The distribution of each element in the individual particles was analysed by EDS (Oxford Ultim Max 65, Oxford Instruments) for element line profile and mapping. We utilized ICP-OES (Optima 4300 DV, PerkinElmer) to measure metal ions leached into the electrolyte. XPS (NEXSA, Thermo Fisher Scientific) was used to analyse changes in the electrode before and after the experiments. For IL-SEM, catalyst was drop-cast onto gold transmission electron microscopy grids for use as a working electrode.

Raman spectroscopy measurements were conducted using a Horiba Xplora microscope situated within a custom-built PEEK cell, as depicted in Fig. 5b. Observations were made using a 60× water immersion lens (LUMPLFLN60XW). Calibration of the Raman frequency was achieved with a silicon wafer reference (520.6 cm^{-1}). The experimental set-up included a 532-nm laser and an 1,800 lines mm^{-1} grating monochromator for light dispersion. Signal detection was performed with a 10-s integration time over 10 cumulative scans. Electrochemical measurements utilized a platinum coil as the counter-electrode and featured Ag/AgCl as the reference and catalyst-coated gold substrates as the working electrodes.

Electrochemical experiments

All electrochemical CO_2RR experiments were performed in a zero-gap cell. An anode and cathode with geometric areas of 9 cm^2 were placed between two current collectors; CuP$_2$ was used as the cathode catalyst, and Pt/C (1 mg cm^{-2}, 46.7%, TKK) airbrushed on a gas diffusion layer (MGL190, AvCarb) was used as the anode. An anion-exchange membrane (PiperION 20 nm, Versogen) was used after activation in 1-M KOH for 24 h. Gold-coated titanium single serpentine flow fields were used as the cathode and anode. To prevent leakage of the electrolyte and minimize the resistance in the MEA, a rubber gasket (630 μm) was utilized. All the components were assembled within an electrolyser, with a torque wrench being used to secure the screws to a tightness of 60 N·m. The anode was supplied with 1-M KOH electrolyte (at room temperature) at a flow rate of 18 ml min^{-1}, and humidified CO_2 (60 °C, with 100% relative humidity) was supplied to the cathode at a flow rate of 500 sccm. A chiller, circulating water at 5 °C, was connected to the outlet of the cathode to liquefy the vaporized products. We applied constant currents of -100 mA cm^{-2} to -1.1 A cm^{-2} for 4 h using a potentiostat/galvanostat (PGSTAT30, Autolab), for the CO_2 reduction experiments. The liquid-phase products were quantified using

headspace GC-MS (Agilent Technologies). Subsequently, the FE values of each product were calculated.

Data availability

Data supporting the findings of this study are available from the corresponding authors upon reasonable request. Source data are provided with this paper.

References

1. Daehn, K. et al. Innovations to decarbonize materials industries. *Nat. Rev. Mater.* **7**, 275–294 (2021).
2. Qi, K. et al. Unlocking direct CO_2 electrolysis to C_3 products via electrolyte supersaturation. *Nat. Catal.* **6**, 319–331 (2023).
3. O'Brien, C. P. et al. Single pass CO_2 conversion exceeding 85% in the electrosynthesis of multicarbon products via local CO_2 regeneration. *ACS Energy Lett.* **6**, 2952–2959 (2021).
4. Alabdullah, M. et al. One-step conversion of crude oil to light olefins using a multi-zone reactor. *Nat. Catal.* **4**, 233–241 (2021).
5. Lee, S., Choi, M. & Lee, J. Looking back and looking ahead in electrochemical reduction of CO_2. *Chem. Rec.* **20**, 89–101 (2020).
6. Park, G., Hong, S., Choi, M., Lee, S. & Lee, J. Au on highly hydrophobic carbon substrate for improved selective CO production from CO_2 in gas-phase electrolytic cell. *Catal. Today* **355**, 340–346 (2020).
7. Choi, M. et al. Syngas production for Fischer–Tropsch process via co-electrolytic processes of CO_2 reduction and NH_3 oxidation. *Chem. Eng. J.* https://doi.org/10.1016/j.cej.2021.132563 (2022).
8. Creel, E. B. & McCloskey, B. D. Scalable CO_2-to-oxygenate production. *Nat. Catal.* **1**, 6–7 (2018).
9. Xie, Y. et al. High carbon utilization in CO_2 reduction to multi-carbon products in acidic media. *Nat. Catal.* **5**, 564–570 (2022).
10. Garcia D. A. et al. CO_2 electrolysis to multicarbon products at activities greater than 1 A cm^{-2}. *Science* https://doi.org/10.1126/science.aay4217 (2020).
11. Huang, J. E. et al. CO_2 electrolysis to multicarbon products in strong acid. *Science* **372**, 1074–1078 (2021).
12. Chen, Y. et al. Efficient multicarbon formation in acidic CO_2 reduction via tandem electrocatalysis. *Nat. Nanotechnol.* https://doi.org/10.1038/s41565-023-01543-8 (2023).
13. Zhuang, T.-T. et al. Steering post-C–C coupling selectivity enables high efficiency electroreduction of carbon dioxide to multi-carbon alcohols. *Nat. Catal.* **1**, 421–428 (2018).
14. Wen, G. et al. Continuous CO_2 electrolysis using a CO_2 exsolution-induced flow cell. *Nat. Energy* **7**, 978–988 (2022).
15. Gu, Z. et al. Efficient electrocatalytic CO_2 reduction to C_{2+} alcohols at defect-site-rich Cu surface. *Joule* **5**, 429–440 (2021).
16. Miao, R. K. et al. Electroosmotic flow steers neutral products and enables concentrated ethanol electroproduction from CO_2. *Joule* **5**, 2742–2753 (2021).
17. Lee, M. G. et al. Selective synthesis of butane from carbon monoxide using cascade electrolysis and thermocatalysis at ambient conditions. *Nat. Catal.* **6**, 310–318 (2023).
18. Xu, Y. et al. Self-cleaning CO_2 reduction systems: unsteady electrochemical forcing enables stability. *ACS Energy Lett.* **6**, 809–815 (2021).
19. Zhang, R. et al. Synthesis of *n*-propanol from CO_2 electroreduction on bicontinuous Cu_2O/Cu nanodomains. *Angew. Chem. Int. Ed.* **63**, e202405733 (2024).
20. She, X. et al. Pure-water-fed, electrocatalytic CO_2 reduction to ethylene beyond 1,000 h stability at 10 A. *Nat. Energy* **9**, 81–91 (2024).
21. Lee, W., Kim, Y. E., Youn, M. H., Jeong, S. K. & Park, K. T. Catholyte-free electrocatalytic CO_2 reduction to formate. *Angew. Chem. Int. Ed.* **57**, 6883–6887 (2018).
22. Xing, Z., Hu, L., Ripatti, D. S., Hu, X. & Feng, X. Enhancing carbon dioxide gas-diffusion electrolysis by creating a hydrophobic catalyst microenvironment. *Nat. Commun.* **12**, 136 (2021).
23. Vennekötter, J.-B., Scheuermann, T., Sengpiel, R. & Wessling, M. The electrolyte matters: stable systems for high rate electrochemical CO_2 reduction. *J. CO2 Util.* **32**, 202–213 (2019).
24. Lee, J. et al. Catholyte-free electroreduction of CO_2 for sustainable production of CO: concept, process development, techno-economic analysis, and CO_2 reduction assessment. *Green Chem.* **23**, 2397–2410 (2021).
25. Zhu, P. & Wang, H. High-purity and high-concentration liquid fuels through CO_2 electroreduction. *Nat. Catal.* **4**, 943–951 (2021).
26. Choi, M., Bong, S., Kim, J. W. & Lee, J. Formation of 1-butanol from CO_2 without *CO dimerization on a phosphorus-rich copper cathode. *ACS Energy Lett.* **6**, 2090–2095 (2021).
27. Seger, B., Robert, M. & Jiao, F. Best practices for electrochemical reduction of carbon dioxide. *Nat. Sustain.* **6**, 236–238 (2023).
28. Weekes, D. M., Salvatore, D. A., Reyes, A., Huang, A. & Berlinguette, C. P. Electrolytic CO_2 reduction in a flow cell. *Acc. Chem. Res.* **51**, 910–918 (2018).
29. Calvinho, K. U. D. et al. Selective CO_2 reduction to C_3 and C_4 oxyhydrocarbons on nickel phosphides at overpotentials as low as 10 mV. *Energy Environ. Sci.* **11**, 2550–2559 (2018).
30. Kang, S. et al. Durable nickel–iron (Oxy)hydroxide oxygen evolution electrocatalysts through surface functionalization with tetraphenylporphyrin. *Angew. Chem. Int. Ed.* **61**, e202214541 (2022).
31. Cheng, C. et al. Amorphous $Sn(HPO_4)_2$-derived phosphorus-modified Sn/SnO core/shell catalyst for efficient CO_2 electroreduction to formate. *J. Energy Chem.* **81**, 125–131 (2023).
32. Bale, C. W. et al. FactSage thermochemical software and databases, 2010–2016. *Calphad* **54**, 35–53 (2016).
33. Delmo, E. P. et al. The role of glyoxal as an intermediate in the electrochemical CO_2 reduction reaction on copper. *J. Phys. Chem. C* **127**, 4496–4510 (2023).
34. David, A. K. et al. Combined computational and experimental investigation on the mechanism of CO_2 hydrogenation to methanol with Mn-PNP-pincer catalysts. *ACS Catal.* **12**, 15310–15322 (2022).
35. Shyama, C. M. et al. A computational study on ligand assisted vs. ligand participation mechanisms for CO_2 hydrogenation: importance of bifunctional ligand based catalysts. *Phys. Chem. Chem. Phys.* **21**, 3932–3941 (2019).
36. Bhaskar, M. et al. Toward rational design of 3*d* transition metal catalysts for CO_2 hydrogenation based on insights into hydricity-controlled rate-determining steps. *Inorg. Chem.* **55**, 5438–5444 (2016).
37. Tang, M. T., Peng, H.-J., Stenlid, J. H. & Abild-Pedersen, F. Exploring trends on coupling mechanisms toward C_3 product formation in CO_2R. *J. Phys. Chem. C* **125**, 26437–26447 (2021).
38. Cronin, S. P. et al. Direct synthesis of 1-butanol with high Faradaic efficiency from CO_2 utilizing cascade catalysis at a Ni-enhanced $(Cr_2O_3)_3Ga_2O_3$ electrocatalyst. *J. Am. Chem. Soc.* **145**, 6762–6772 (2023).
39. Li, Z. & Wu, J. Co-electrolysis of CO_2 and formaldehyde to ethanol: an inspiring asymmetric C–C coupling pathway. *Chem Catal.* **2**, 2808–2810 (2022).
40. Yan, T. et al. Multiscale CO_2 electrocatalysis to C_{2+} products: reaction mechanisms, catalyst design, and device fabrication. *Chem. Rev.* **123**, 10530–10583 (2023).
41. Liu, L., Ye, X. P. & Bozell, J. J. A comparative review of petroleum-based and bio-based acrolein production. *ChemSusChem* **5**, 1162–1180 (2012).
42. Lan, X., Wang, T., Li, X., Huang, N. & Wang, J. $Pt@SnO_x/SiO_2$ catalysts with enhanced selectivity to allyl alcohol for acrolein hydrogenation. *Catal. Sci. Tech.* **6**, 7703–7707 (2016).

Competing interests

The authors declare no competing interests.

Additional information

Supplementary information The online version contains supplementary material available at https://doi.org/10.1038/s41929-025-01341-6.

Correspondence and requests for materials should be addressed to Jaeyoung Lee.

Peer review information *Nature Catalysis* thanks the anonymous reviewers for their contribution to the peer review of this work.

Reprints and permissions information is available at www.nature.com/reprints.

Publisher's note Springer Nature remains neutral with regard to jurisdictional claims in published maps and institutional affiliations.